PERGAMON

Journal of Structural Geology 26 (2004) 307–324

JOURNAL OF STRUCTURAL GEOLOGY

www.elsevier.com/locate/jsg

Analogue models of melt-flow networks in folding migmatites[1]

Joseph Barraud*, Véronique Gardien, Pascal Allemand, Philippe Grandjean

Laboratoire Dynamique de la Lithosphère, Université Claude Bernard—ENS LYON, UMR 5570, 2 rue Dubois, Bat. GEODE, 69622 Villeurbanne Cedex, France

Received 11 October 2001; received in revised form 28 May 2003; accepted 2 June 2003

Abstract

We have modelled the formation and the layer-parallel shortening of layered (stromatic) migmatites. The model consists of thin superposed layers of partially molten microcrystalline wax. The melt (30 vol.%) has a negative buoyancy and a high viscosity contrast with its solid matrix. As soon as the shortening begins, melt-filled veins with high aspect ratios open along foliation. The melt is segregated into the veins, forming a stromatic layering. During incipient folding, crescent-shaped saddle reefs open at the hinges of open sinusoidal folds. Further shortening and melt-enhanced shear displacements on interlayer interfaces cause chevron folds to develop and the saddle reefs to become triangular. In comparison, a melt-free experiment shows only a few layer-parallel openings and no saddle reefs in chevron folds. On the basis of our experimental results, we propose that in migmatites: (1) mesoscale melt migration is a combination of flow in immobile veins and movements of veins as a whole; (2) the changes in the geometry of the mesoscale melt-flow network create the pressure gradients that drive melt migration; (3) the melt-flow network does not need to be fully interconnected to allow local expulsion; (4) melt expulsion is episodic because the temporal evolution of the network combines with the spatial heterogeneity of the deformation.
© 2003 Elsevier Ltd. All rights reserved.

Keywords: Migmatites; Melt segregation; Melt migration; Compaction; Leucosomes; Folds; Paraffin wax

1. Introduction

During orogenesis transfer of matter in the form of solute phases in aqueous fluids (e.g. Oliver, 1996) or as silicate melt (e.g. Brown, 1994) takes place in the continental lithosphere. Generation of granite melts and their transfer from the lower/middle crust to the upper crust is a complex sequence of physical and chemical processes that occur at different scales and different rates (Brown, 1994; Handy et al., 2001; Vanderhaeghe, 2001). Melt production in anatectic domains is between 10 and 50 vol.%, but more often at the lower end of this range (e.g. Thompson, 1996; Milord et al., 2001). The volume of the source region of granite melts is therefore much larger than the volume of a pluton and a very efficient mechanism must occur to separate the melt from its initial grain-scale site of melting.

In this paper, we call *segregation* the first movement of melt from primary pools that form between reacting minerals to nearby sites that are at least one order of magnitude larger. Tremendous work has been made on this process: analytical modelling (McKenzie, 1984; Sleep, 1988; Ricard et al., 2001), analogue experiments (Rosenberg and Handy, 2000), numerical models (Simakin and Talbot, 2001) and field observations (e.g. Sawyer, 2001; Marchildon and Brown, 2003). The broad consensus is that deformation plays a major role in increasing compaction rate, in providing melt pathways and spaces to fill in. As shown by Handy et al. (2001), segregation is a dynamic process that depends mainly on strain and strain rate and little on melt fraction. Grain boundary sliding, shear band formation or microfracturing allow melt to move within the deforming rock, even at very low melt fractions (<5 vol.%; Rosenberg and Handy, 2000). These results led Handy et al. (2001) to consider that, in a dynamic context, melt will always leave an open system. However, porous flow may transport melt on very short distances, of the order of

[1] Movies are available on Science Direct in the *online version of this paper*

* Corresponding author. Current and correspondence address: Department of Earth Sciences, University of Cambridge, Downing Street, Cambridge CB2 3EQ, UK. Tel.: +44-1223-333433; fax: +44-1223-333450.

E-mail address: jbar02@esc.cam.ac.uk (J. Barraud).

0191-8141/$ - see front matter © 2003 Elsevier Ltd. All rights reserved.
doi:10.1016/j.jsg.2003.06.002

magnitude of the compaction length (McKenzie, 1984). In granitic systems, the latter is between 1 cm and 1 m only (Petford, 1995; Ricard et al., 2001). Segregation is therefore not *extraction*, and the melt that fills dilatant shear surfaces or opening veins has still great distances to travel before resting in a pluton.

Several recent geochemical studies of migmatitic and granulitic domains have shown that part of the melt (up to about 60 vol.%) may leave the system after segregation (Nyman et al., 1995; Kriegsman, 2001; Milord et al., 2001; Solar and Brown, 2001; White and Powell, 2002). Field observations in migmatites allow us to investigate melt flow at scales from tens of centimetres to hundreds of metres. In this paper, this range of length scales is termed the *mesoscale*. We define melt *migration* as a mesoscale viscous flow of liquid within the volume of the anatectic unit. Migration occurs until melt escapes out of the source region. We will then call it an *expelled* melt, resulting from an *expulsion*. These expressions are here preferred to 'extracted melt' and 'extraction' that imply external forces draining the partially molten source. The aim of all these definitions is to emphasize that these words should be used carefully because the processes of segregation, migration, expulsion and final ascent are different in terms of length and time scales.

Mainly based on field observations in migmatites, the pervasive migration models of Brown and Solar (1999), Vanderhaeghe (1999) and Weinberg (1999) suggest that melt flows through an interconnected macroscopic network of concordant and discordant veins. These veins are now frozen as leucosomes, which commonly do not show melt compositions, but "represent the cumulate products of fractional crystallization and variable melt loss of evolved fractionated liquid" (Solar and Brown, 2001). Nevertheless, melt flow in the veins was probably much faster than grain-scale porous flow (Rutter and Neumann, 1995). Although various models on pervasive melt migration have been proposed (Sleep, 1988; Rutter and Neumann, 1995; Handy et al., 2001), there is a lack of experimental studies on the processes of mesoscale syntectonic melt migration in migmatites.

Many questions remain open: what are the orientation, position, and shape of melt pathways in a heterogeneous and anisotropic system such as migmatites? Which amount of deformation is needed to form an interconnected network of melt pathways and trigger-melt expulsion? Once an interconnected network is created, does the melt move easily through it or does it need tectonic assistance to migrate? Does this network really need to be interconnected? Is expulsion continuous or discontinuous in time? To answer these questions, it is imperative to visualize the initiation and development of the melt-filled structures during shortening. An estimate of the melt content at each increment of the deformation is necessary. Analogue modelling can further develop our understanding of these issues because progressive deformation of the models can be observed almost continuously.

Barraud et al. (2001a,b) have shown that partially molten paraffin wax can be used to perform analogue modelling of the deformation of migmatites. The present paper shows two new experiments, which were designed to study the effects of melt on folding of a multilayer. A melt-free experiment is compared with a melt-bearing one. The role of melting on the rheology was scaled qualitatively in terms of strength reduction and strain localization. Moreover, the evolution of the melt-flow network and the progression of the melt expulsion were recorded during horizontal shortening of the partially molten model. In conclusion, we will propose a conceptual model of the melt segregation and migration in folding migmatites that takes into account the temporal evolution of the mesoscale melt-flow network.

2. Experimental conditions

2.1. Analogue material

In both experiments described below, the analogue material is microcrystalline paraffin wax, which offers the possibility of simulating the melting reaction and therefore a progressive change from solid to liquid state. Indeed, the fact that metamorphic reactions are seldom reproduced is a well-known limitation of analogue experiments.

Paraffin waxes are composed of alkane macromolecules C_nH_{2n+2} with n from 14 to 70. Their crystallography shows a molecular lamellar structure (Dorset, 1997). Microcrystalline paraffin wax is chemically more complex than the macrocrystalline paraffin waxes that have been previously used by several workers to reproduce small-scale structures such as folds, boudins or shear zones (Neurath and Smith, 1982; Abbassi and Mancktelow, 1992; Grujic and Mancktelow, 1995). Consequently, their melting behaviours are different. Macrocrystalline waxes are defined by a single melting point and this means that only 1 or 2 °C separates their solidus and liquidus temperatures. In contrast, we measured (see below) well-distinct solidus and liquidus temperatures for microcrystalline wax: about 40 and 80 °C, respectively. At an intermediate temperature, microcrystalline wax is a two-phase material, consisting of a liquid phase and a solid viscous phase. In the following section microcrystalline paraffin wax is simply called *wax*.

The melt fraction of partially molten wax has been measured as a function of temperature with an optical microscope using an adapted fluid-inclusion heating stage. The temperature was set with a precision of about 0.1 °C. A very thin layer of wax was obtained by pouring a drop of melted wax onto a transparent plate. Fig. 1a shows a cross-polarised transmitted light microphotograph of crystals of wax at room temperature. The crystals formed a complex pattern of strongly birefringent needles. Dark areas were either crystals at extinction or not very well crystallized

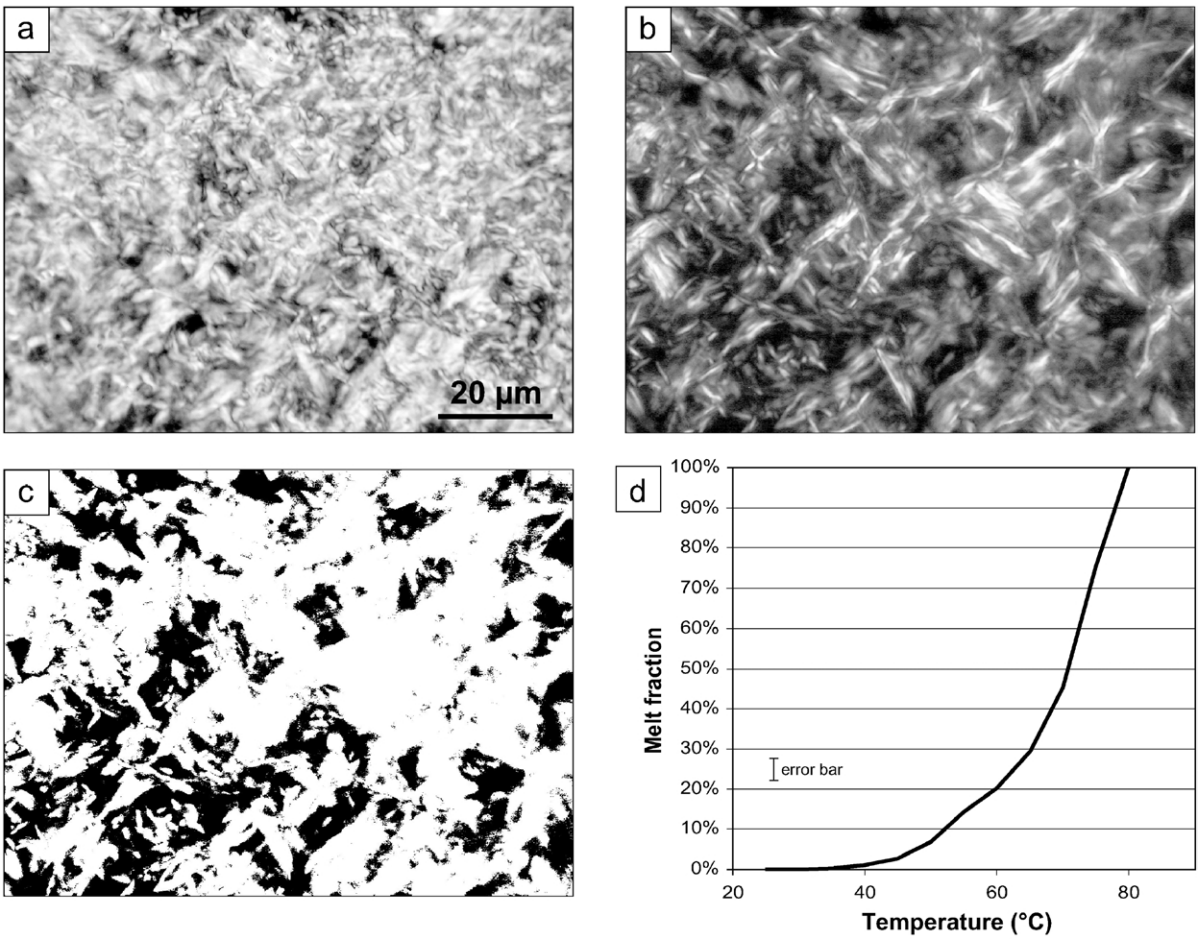

Fig. 1. (a) and (b) Cross-polarised transmitted light microphotographs of a thin layer (<0.5 mm) of microcrystalline wax. (a) At 20 °C, the crystals form a complex pattern of strongly birefringent needles. Black spots are holes or not well-crystallised wax. (b) At 65 °C, wax is partially molten. New black pools are isotropic melt. (c) A bitmap picture was obtained by thresholding the halftone picture (b) and shows melt in black and crystals in white. At 65 °C, the melt fraction is 30 ± 3 vol.%. (d) The curve of the melt fraction vs. temperature was obtained by repeating this process between 25 and 80 °C every 5 °C.

wax. With increasing temperature, the wax began to melt and new black spots consisting of isotropic melt developed (Fig. 1b). The melt fraction was measured by comparing the grey level histograms of the digital pictures: as the melt fraction increased, the amount of dark pixels in the picture increased, too. A bitmap picture was then acquired by thresholding and shows melt in black and crystals in white (Fig. 1c). By measuring the proportion of black pixels at different steps of melting, we obtained the curve of the melt fraction vs. temperature (Fig. 1d). At 65 °C, which is the temperature of the melt-bearing experiment described below, the melt fraction was 30 ± 3 vol.%.

The topology of the melt at the grain scale before deformation is shown by the microphotograph of partially molten wax (Fig. 1b and c). The length of the wax crystals is between 10 and 20 microns (Fig. 1b). At 65 °C, the melt pockets are between 5 and 15 microns in diameter and are homogeneously distributed in wax before deformation (Fig. 1b and c). This mimics the natural melt pools that develop at the boundaries between appropriate minerals (Gardien et al., 1995; Sawyer, 2001). The high melt fraction (30 vol.%), the apparent 2D interconnection (Fig. 1c) and the observation that melt percolated through the solid matrix during the experiments (see below) suggest that melt was interconnected.

The rheology of wax has been investigated in simple uniaxial compression tests for temperatures between 58 and 70 °C, which correspond to melt fractions between 0.17 and 0.45. A constant load has been applied on cylindrical samples and the strain rate has been measured. A typical strain-time plot shows (Fig. 2): (1) an early transient stage of fast deformation that corresponds to the loading of the sample, (2) a period of shortening at constant strain rate, and (3) a period of accelerating deformation that led to the breakdown of the sample along several shear fractures. Even if the melt fraction was as high as 0.45, the mechanical behaviour was still dominated by the solid matrix and the strength drop only occurred at shortening percentages higher than 15–20%. During the second stage, an effective viscosity (ratio between stress and strain rate) can be defined and measured. The relative precision of these simple measurements is about 10–15%. From 58 to 70 °C, the

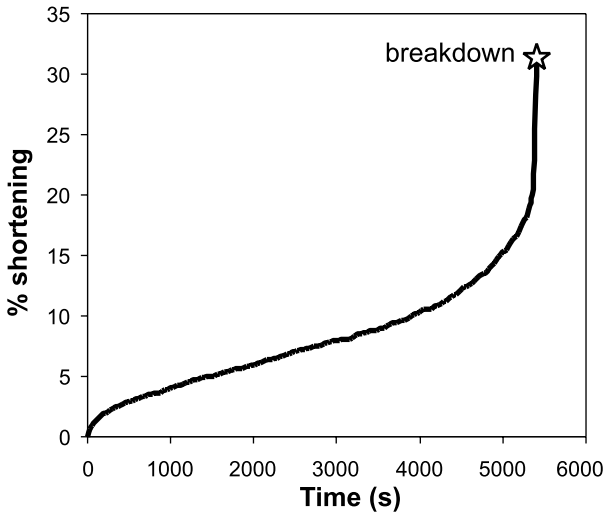

Fig. 2. Rheology of microcrystalline wax. The strain-time plot shows the result of a uniaxial test at 70 °C (melt fraction 0.45) and constant stress. The first stage of accelerating deformation corresponds to the initial loading. The period of shortening at constant strain rate allows us to define an effective viscosity of 4×10^7 Pa s. The final stage consisted of the breakdown of the sample along a shear fracture.

viscosity decreases from 2×10^9 to 4×10^7 Pa s. At 65 °C, it is 10^8 Pa s for strain rates between 4×10^{-5} and 4×10^{-6} s^{-1}, which are close to the mean strain rate of our analog experiments (3×10^{-6} s^{-1}).

At 65 °C, the measured viscosity of partially molten wax is 10–11 orders of magnitude higher than the viscosity of the liquid alone, which is 10^{-2}–10^{-3} Pa s (supplier's documentation). The viscosity contrast between melt and solid matrix was therefore even larger, *at least* 10 orders of magnitude.

2.2. Experimental apparatus

The experimental apparatus consists of a Plexiglas box, 350 mm long, 150 mm wide and 250 mm high with one mobile wall fixed to a screw jack. This screw jack is coupled to an electric motor through a reducer. The box contains the wax model and is placed in a water tank. The water was maintained at a constant temperature. A polystyrene case surrounded this apparatus to minimize large thermal gradients. Although the latter are of the order of 3 °C between the bottom and the top of the wax layer, their effect is not visible during experiments. As the heat capacity of wax is high (3 J g^{-1} $°C^{-1}$), temperature was stable and this allows the insulating case to be temporarily removed to photograph the state of deformation without cooling the model.

The width of the box was slightly oversized compared with the width of the wax layers. There were therefore two tiny vertical spaces, 1 mm wide, between the model and the front and back vertical sides of the box. These spaces tended to wane rapidly during deformation as the horizontal shortening made the layers widen laterally. The horizontal widening was 1.3% after about 5–7% of shortening. After this early stage, conditions of plane strain were achieved. However, the joint of the mobile wall was neither waterproof nor 'waxproof', allowing water or melt to move from the box containing the model to the water tank. The system was thus considered as open throughout the experiments.

2.3. Construction of the models

The model simulated a horizontally foliated layer of high-grade rocks. Depending on the scale factor (see next section), the model may correspond in nature to a single layer, about 1 m thick, or to a metamorphic unit, a few hundreds of meters thick. In order to reproduce a strong mechanical planar anisotropy, the wax layer in both experiments was made of 13 superposed thin laminae (5–6 mm thick) that are called 'sub-layers' thereafter. This stack was initially 68 mm thick, 250 mm long and 150 mm wide.

Each sub-layer was molded over the previous one by pouring hot molten wax into a rectangular mould. During cooling, the sub-layer adhered to its neighbour, producing a weak welding. After installation in the experimental box, the stack was annealed at the chosen temperature for 2 days. In the case of suprasolidus temperatures, this assures a homogeneous distribution of melt before deformation.

An upper layer of sand, 10 cm thick, increased the vertical stress in the model and simulated the lithostatic load (see below). A plastic film separated the sand from the wax. The mobile wall had a constant velocity of 2.4 mm h^{-1} but the motor had to be stopped overnight. These intervals allowed us to investigate the influence of shortening on the expulsion rate. The average deformation rate was around 3×10^{-6} s^{-1}. A photograph was taken every hour throughout the experiments. Movies were then created to allow an easier visualization of the progressive deformation (available on the *Journal of Structural Geology* web site).

2.4. Scaling of the experiments

The scaling of our experiments is based on relevant non-dimensional ratios linking geometric, kinematic and dynamic quantities (Ramberg, 1981; Barraud et al., 2001a,b). If the model is geometrically similar to the initial state of the natural structure, the kinematic similarity arises from the dynamic similarity (Ramberg, 1981). After Ramberg (1981), "structures are *dynamically similar* if the ratio is constant between the various kinds of mechanical forces, compared kind for kind, that act on any two corresponding particles in original and model". That is:

$$F^* = \frac{F_{1,0}}{F_{1,\mathrm{m}}} = \frac{F_{2,0}}{F_{2,\mathrm{m}}} = \cdots = \frac{F_{k,0}}{F_{k,\mathrm{m}}} \quad (1)$$

where F_1, F_2, …, F_k are the various forces acting on the

system. Here and in the following paragraphs, the subscripts 0 and m stand for nature and model, respectively.

To simplify the scaling calculation, we must consider migmatites as Newtonian materials. Non-linear properties such as melt segregation, shear localization, strain hardening or softening are expected in partially molten rocks (e.g. Vigneresse and Tikoff, 1999; Handy et al., 2001). However, our analogue material reproduces these kinds of behaviour only qualitatively (see above tests and Barraud et al. (2001a)).

To achieve dynamic similarity, we will thus consider only buoyancy forces, the viscous force and the lithostatic load. The model and the prototype are both exposed to the same gravitational field so that buoyancy forces are not correctly scaled (Ramberg, 1981). However, the ratio of the density of the solid to the density of the liquid is the same in the experiments and in natural systems (Table 1). This means that buoyant melt can move upward in our experiments, but not fast enough for a correct scaling.

The viscous force ηVl is the force needed to deform a cube of length l and viscosity η at a constant shortening velocity V. A large range of viscosities ($\eta = 10^{16}$–10^{20} Pa s) seems reasonable to account for the variability of melt fractions, modal composition, and grain size of migmatites (Brown et al., 1995; Rutter and Neumann, 1995; Talbot, 1999). The lithostatic load is the weight of the column of height h. Let Ψ be the ratio between these two forces:

$$\Psi = \frac{\rho g h l^2}{\eta V l} = \frac{\rho g h l}{\eta V} \tag{2}$$

The density ρ is here a mean value for the rocks lying above the migmatites. For the model, the values of the physical parameters are fixed by the scale of the laboratory and by the properties of the analogue materials (Table 1). For the melt-bearing experiment, at 65 °C, $\Psi_m = 3$. For nature, because of the variability of the natural settings (Table 1), different combinations of viscosity, length and velocity values suit the requirement $\Psi_0 = \Psi_m$. An original approach consists therefore in finding the natural settings that best fit the model, allowing a better understanding of the role played by each parameter. To achieve the similarity, we thus need:

$$\Psi_0 = \frac{\rho_0 g h_0 l_0}{\eta_0 V_0} = \Psi_m = 3 \tag{3}$$

The depth h_0, the gravitational acceleration g and the density ρ_0 are not subject to great variations with the geological context and can be considered as constant.We obtain:

$$l_0 = \frac{\eta_0 V_0 \Psi_m}{\rho_0 g h_0} \tag{4}$$

and

$$\dot{\epsilon}_0 = \frac{V_0}{l_0} = \frac{\rho_0 g h_0}{\eta_0 \Psi_m} \tag{5}$$

where $\dot{\epsilon}_0$ is the initial strain rate. For $h_0 = 20$ km and $\rho_0 = 2800$ kg m^{-3}, l_0 is plotted as a function of η_0 and corresponding values of $\dot{\epsilon}_0$, for various values of V_0 (Fig. 3). This diagram shows lines on which suitable combinations of parameters can be found: for example, our model correctly reproduces layers deforming at 1 mm year^{-1}, that are 17 m long and have a viscosity of 10^{17} Pa s, which gives a strain rate of 10^{-12} s^{-1}. At 0.1 mm year^{-1}, the viscosity should be higher (10^{18} Pa s), or even higher (10^{19} Pa s) if hectometric structures are considered. These values are in the likely ranges estimated for migmatitic domains (Vigneresse et al., 1996; Brown and Solar, 1999; Talbot, 1999; Simakin and Talbot, 2001; Vanderhaeghe, 2001). Nevertheless, some

Table 1
Physical parameters controlling the melt-migration processes in nature and in the model

	Symbol	Units	Nature	Model
Length	l	m	0.1–1000	0.2
Depth	h	m	$12–50 \times 10^3$	0.1
Shortening velocity	V	m y^{-1}	10^{-6}–10^{-2}	20
Strain rate	$\dot{\epsilon}$	s^{-1}	10^{-12}–10^{-14}	3×10^{-6}
Density of the solid	ρ_s	kg m^{-1}	2800–3000	950
Density of the liquid	ρ_m	kg m^{-1}	2400–2500	820
ρ_s/ρ_m	–	–	1.12–1.25	1.2
Viscosity of the partially molten material	η_s	Pa s	10^{16}–10^{20}	10^8
Viscosity of the liquid	η_m	Pa s	10^4–10^6	10^{-2}–10^{-3}
η_s/η_m	–	–	10^{10}–10^{14}	10^{10}–10^{11}

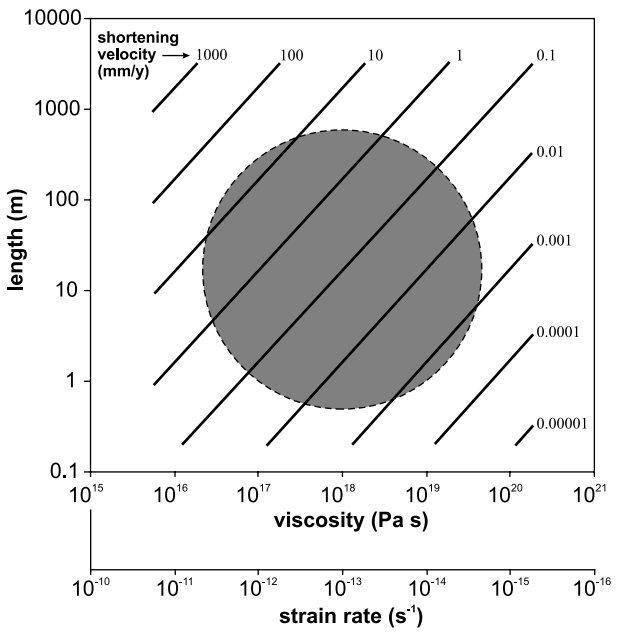

Fig. 3. Characteristic length vs. viscosity of natural migmatites modelled by partially molten wax. The curves are plotted for varying values of shortening velocity. Corresponding strain rates are shown. A point on a curve represents a geological context that is correctly reproduced by our experimental model. The circle encloses the most realistic combinations of parameters.

extreme combinations are not possible because they lead to unrealistic strain rate or viscosities (Fig. 3).

In the melt-free experiment, the viscosities of both the analogue material and the corresponding natural prototype are higher. If they increase in the same proportion, the ratios Ψ_m and Ψ_0 remain equal and similarity is achieved. This assumption has not been verified. However, when melt is not present (no viscosity contrast between phases), scaling of the forces is less crucial and only initial conditions and kinematics really matter.

3. Experimental results

3.1. Melt-free experiment

The temperature was set at 40 °C so that the wax had a viscous behaviour but did not melt. Dark water-drops were initially present in the sideways spaces but they rapidly disappeared with the beginning of shortening (Fig. 4 and *melt-free experiment* movie in the *online version of this paper*). Vertical thickening essentially occurred in front of the mobile wall by bending of the upper sub-layers. Rounded sinusoidal folds developed in the six lower sub-layers by 13% shortening (Fig. 4b). As shortening continued these folds transformed to chevrons by sharpening of the hinge and straightening of the limbs (Fig. 4c and d). Five layer-parallel voids opened by 20% shortening in the large hinge zone of the gentle syncline that bordered the mobile wall. Opening of space was due to different radii of curvature in bends of adjacent layers.

3.2. Melt-bearing experiment

As the temperature was constant and well-above the solidus (65 °C) before deformation started, some melt had already segregated from the sides of the model and accumulated in the vertical space between the wax and the box, forming dark lenses or pools that covered about half the layer side surface (Fig. 5a and *melt-bearing experiment* movie in the *online version of this paper*). As the system was open, some melt had also escaped to the water tank and constituted a film on the top of the water (Fig. 5a).

Between 0 and 9% shortening, the initial side boundary melt pools disappeared progressively and thin layer-parallel melt-filled veins opened between the sub-layers (Fig. 5b). The aspect ratio of these veins was around 100. The first buckling instability was noticeable after 9% shortening and folding occurred close to the mobile wall while only little thickening occurred beyond (Fig. 5c–f). Variations in curvature of the sub-layers in fold hinges opened saddle-reef type veins (Figs. 5c and 6). The shape of these veins evolved with progressive deformation. The first ones were crescent-shaped and occupied hinges of open sinusoidal folds (Fig. 5c). Some saddles opened above décollement levels between sub-layers (left-hand lower corner in Fig. 5c) but most of them involved little shear displacements on interfaces. With further shortening, chevron folds formed; the veins acquired a triangular shape and their volume decreased (Fig. 5d).

After 15% shortening, the bending of the sub-layers was so intense that small radial fractures opened in outer arcs of folded sub-layers (Figs. 5d–f and 6). As the folds locked up (23% shortening), discordant horizontal veins opened, producing an incipient disruption of the layering (Figs. 5e and f and 6). Once the limbs of folds rotated to an appropriate angle (about 30–40°), shear displacements on interfaces between sub-layers increased and a few thrusts formed (Fig 5f). Deformation progressively propagated beyond the mobile wall and at the end of the experiment, by 30% shortening, a train of folds had developed.

3.3. Comparison between the melt-free and the melt-bearing experiments

The first obvious difference between the two experiments is the amount of thickening, which is low in the melt-bearing experiment due to a large volume loss (compare Figs. 4 and 5 and see next section). The influence of melting on the mechanical behaviour is manifest, too. During the melt-bearing experiment, the presence of melt resulted in low interlayer cohesion, easy opening of layer-parallel veins and better slip on interfaces. In the melt-free experiment, saddle-reef type voids did not form in the core of the chevron anticlines because opening of layer-parallel veins was precluded by the higher interlayer cohesion and by the vertical stresses produced by the overburden of the sand layer. By comparison, the vertical stresses in the melt-bearing experiment are probably on the level of the melt pressure, which allows the veins to remain open.

3.4. Evolution of melt expulsion

Throughout the melt-bearing experiment melt batches were expelled from the deforming multilayer. At the front and back of the model, they appeared episodically as dark spots and then, with few exceptions, disappeared quickly (in the next 2% of shortening). These spots are melt pools trapped in the vertical sideways spaces existing between the wax and the box. Their size changed at each increment of deformation but most of the time their position was centred on the axial planes of folds. The position of these pools reveals the zones through which the wax layer has lost melt. It is worth noticing that anticlines showed larger melt pools than synclines. This is probably due to the negative buoyancy of the melt.

At 7 and 19% shortening, the motor was stopped but melt expulsion persisted. Indeed, we observed a very slight tightening of the folds (about 1% of contraction). During the second break, a lens of trapped melt, centred on a small saddle reef, widened. This indicates that fold contraction

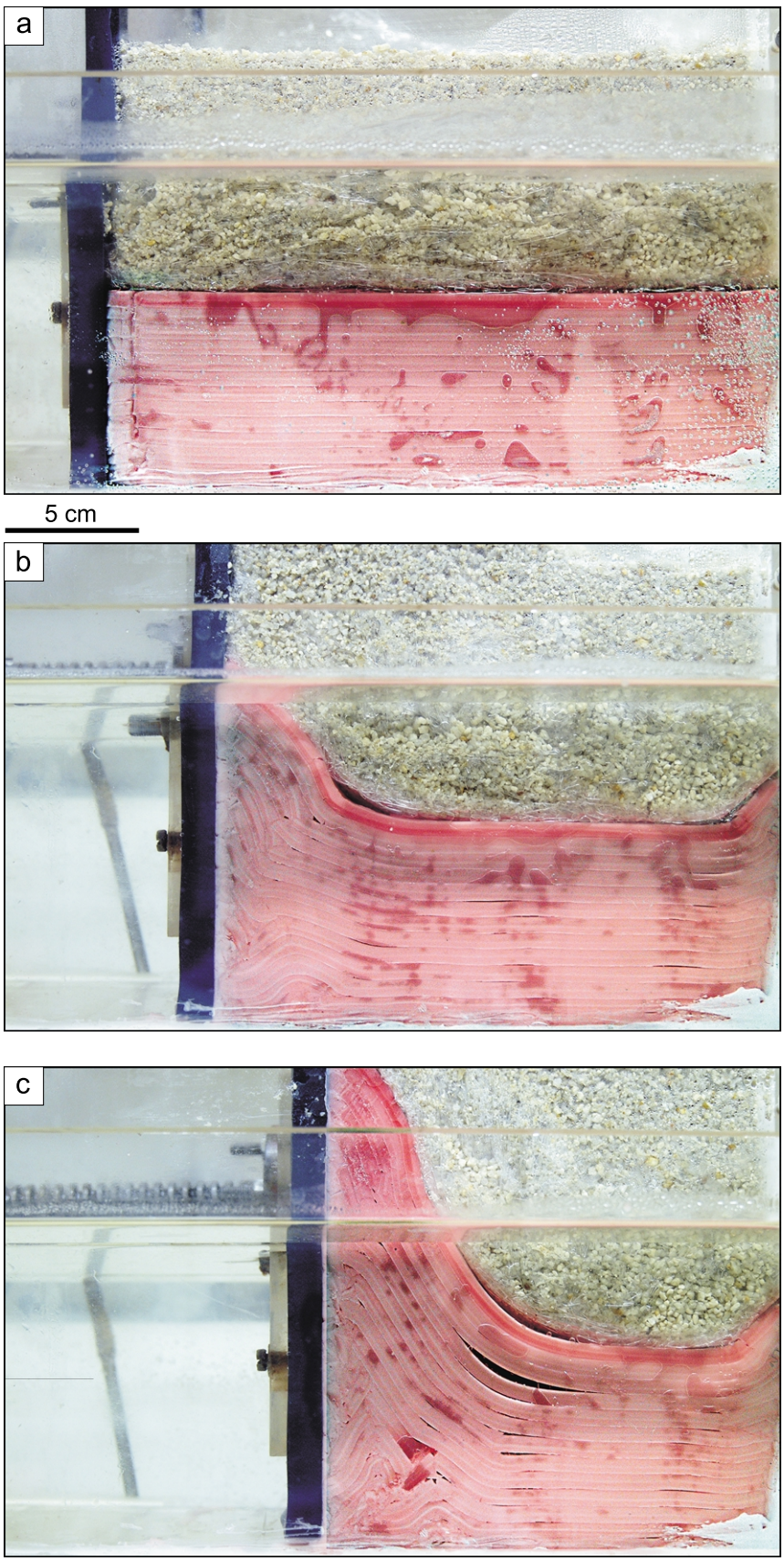
a
5 cm
b
c

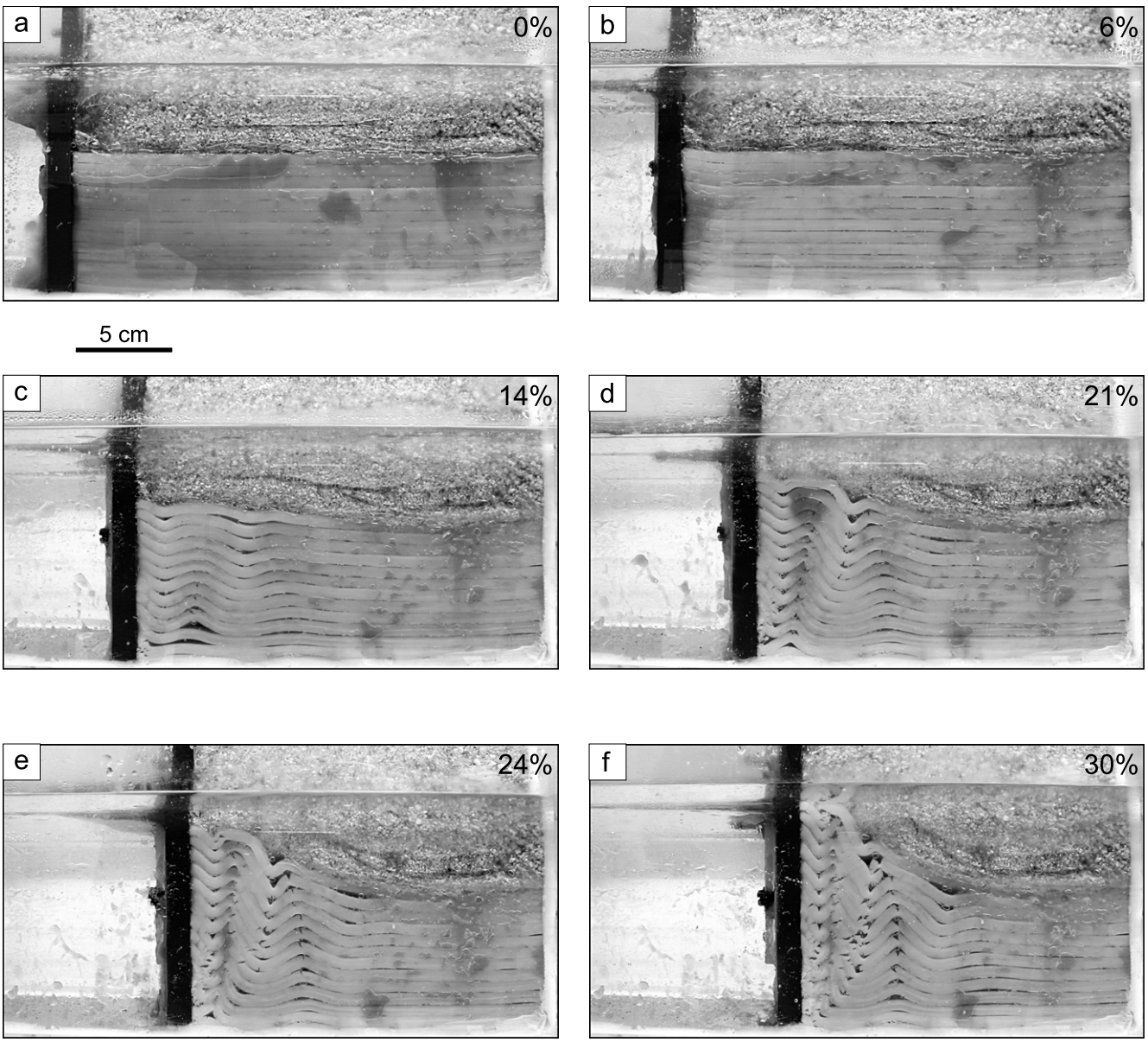

Fig. 5. Melt-bearing experiment. A movie of this experiment is available in the *online version of this paper*. The geometry was identical to the one of the melt-free experiment. The melt fraction was 30 ± 3 vol.%. (a)–(c) During the first percents of shortening, there was almost no thickening. This volume loss corresponded to expelled melt in the water tank. Thin and long melt-filled veins opened between the sub-layers. Folding began at 9% shortening and melt-filled saddle reefs formed in open sinusoidal folds, permitting an effective redistribution of melt. (d)–(f) After 18% shortening, chevron folds formed by sharpening of the hinge and straightening of the limbs. Melt expulsion occurred through the axial planes of anticlines. The expelled melt constituted the dark lenses that covered the side boundaries of the model.

occurred when the melt moved through the saddle reef and escaped.

There are several ways to appreciate how much melt has been expelled from the model: direct and indirect measurements are presented in the following. Melt expulsion implicated a net weight loss of 17.2%. As the initial melt fraction was 30 ± 3 vol.%, 58 ± 5 vol.% of the available melt was thus expelled in the water tank, indicating that the deformation-assisted expulsion of melt was very efficient.

Fig. 4. Melt-free experiment. A movie of this experiment is available in the *online version of this paper*. The model was a multilayer of 13 sub-layers, 5–6 mm thick, so that the stack was 68 mm thick. Temperature was 40 °C. (a) Before deformation. The dark spots on the model side are water drops that seeped through the mobile wall. (b) By 19% shortening thickening occurred essentially in front of the mobile wall. A few layer-parallel cracks opened. Note the absence of saddle reefs in the anticlinal fold (bottom left). (c) Final state (33% shortening). Voids opened essentially between the top layers bent in front of the thickened zone. The width of these voids is higher near the edges than in the core of the model (not visible on this view).

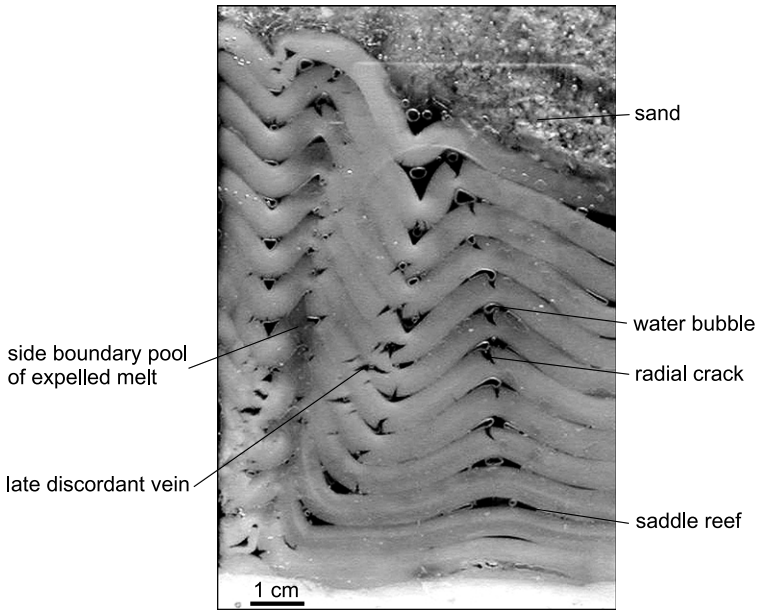

Fig. 6. Melt-bearing analogue model after 27% shortening. The picture is almost full scale and shows the train of folds close to the mobile wall. The amount of lateral shortening increases from right to left. This makes it possible to observe the successive stages of folding, together with the evolution of the position and shape of the melt-filled veins. The water bubbles exist only on the boundaries and not in the interior. They form because water (immiscible with melt) can penetrate into the vertical space between the model and the box.

The mass of escaped molten wax lying on the top of the water after a given increment of deformation (each hour) was collected (Fig. 7). During periods of shortening, the mean extraction rate was 10 g h^{-1}, i.e. a weight loss of 0.5% h^{-1}. In contrast, during periods of no shortening, the mean expulsion rate (averaged to the duration of the break) was 3 g h^{-1}. Immediately after stopping the motor, the expulsion rate fell below 5 g h^{-1}. After restarting the motor, it returned rapidly to a mean value of 10 g h^{-1}. Hence, shortening greatly increased the melt expulsion rate and drove the pumping and expulsion of melt out of the partially molten material. Without shortening melt was expelled slowly at a rate that is likely proportional to the permeability of the model and to the pressure difference between the wax layer and the atmosphere.

During shortening melt expulsion was episodic. This is

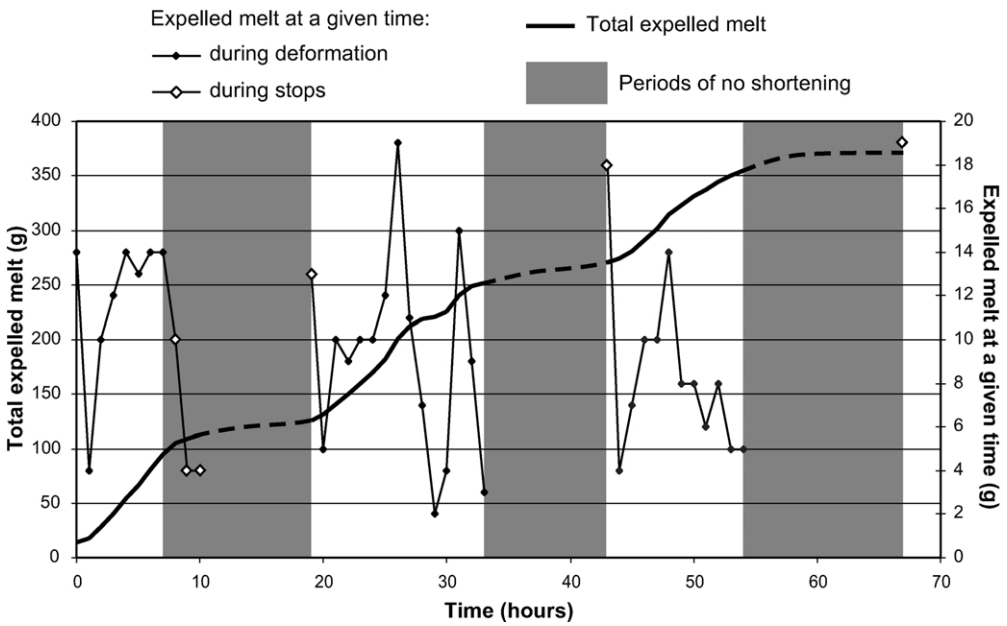

Fig. 7. Melt expulsion during the melt-bearing experiment. The plot shows the mass collected each hour and the total mass of expelled melt vs. time. One hour corresponds to about 1% shortening. The periods in grey are static intervals. The open diamonds on the curve of the collected melt mean that the measure was performed during such an interruption. Shortening considerably accelerated the expulsion, which occurred by a series of pulses.

illustrated by the succession of waxing and waning of vertical lenses of escaping melt is evidence (Fig. 5 and *melt-bearing experiment* movie in the *online version of this paper*). Substantial fluctuations in the expulsion rate occurred with the pulse at 19 g h^{-1} after 13% of shortening, closely followed by a minimum of 2 g h^{-1} (Fig. 7). Consequently, the mechanism of melt movement during folding has to involve episodic processes that are driven by shortening. Before we describe such a model, we present now indirect measurements of melt expulsion.

The area of the front side of the model was digitally measured on photographs (Fig. 8). The previously measured weight loss of the wax layer correlated with its area loss, which is assumed to correspond to the volume loss (Fig. 8). The areas of the right and left parts of the layer were measured separately for comparison (Fig. 8). The area loss close to the mobile wall was systematically higher than the area decrease far from the mobile wall (Fig. 8). Moreover, this contrast increased during the experiment because: (1) the non-folded part far from mobile wall did not lose any more melt after 15% shortening; (2) an acceleration of melt expulsion occurred after 20% shortening corresponding to the lock-up and flattening of the folds (Fig. 5). At the end of the experiment, the area loss of the left and right parts had been 25 and 10%, respectively. Thus, melt expulsion increased with strain and folding accentuated this phenomenon. At the model scale, the melt pathways (layer-parallel veins, saddle reefs, fractured hinges) were more numerous and wider in the folded and more deformed left-hand part of the wax layer, increasing the efficiency of the melt expulsion.

The last evidence of differential melt expulsion within the folded layer takes advantage of the effect of melt depletion on the colour of the wax. The wax was coloured red with an organic dye that is more soluble in the melt. Thus, the melt-enriched wax had a dark colour while the melt-depleted wax was whitened (Figs. 5 and 6) and these variations remain after cooling. A cut was made after the end of a melt-bearing experiment performed in the same conditions as the previously reported one. The cross-section was scanned in half tones and the grey levels were classified into four categories as a function of the depletion in melt. Four colours have then been associated with the four groups to obtain a well-contrasted picture (Fig. 9a). This process emphasises that the folded part of the model lost more melt (about 25% of volume loss) than the non-folded part (about 10 vol.%). The picture shows also the redistribution of the melt within each sub-layer. The outer hinge zones are generally enriched in melt. The same cross-section without colour gradients shows the style of folding of this experiment, similar to the other melt-bearing experiment (Fig. 9b).

4. A model of melt expulsion in a folding melt-bearing multilayer

In the melt-bearing experiment and in others performed in similar conditions, melt expulsion occurs in four stages: (1) melt segregation in veins; (2) redistribution of the melt within the folding layers, the melt generally moving from the limbs to the hinges; (3) deflating of the saddle-type veins and expulsion of the melt sideways, forming waxing melt lenses trapped along the vertical front and back of the model; (4) migration of these melt batches to the water tank. We describe in this section the different driving mechanisms that are involved at each stage.

Melt segregation from the sub-layers to dilatant veins

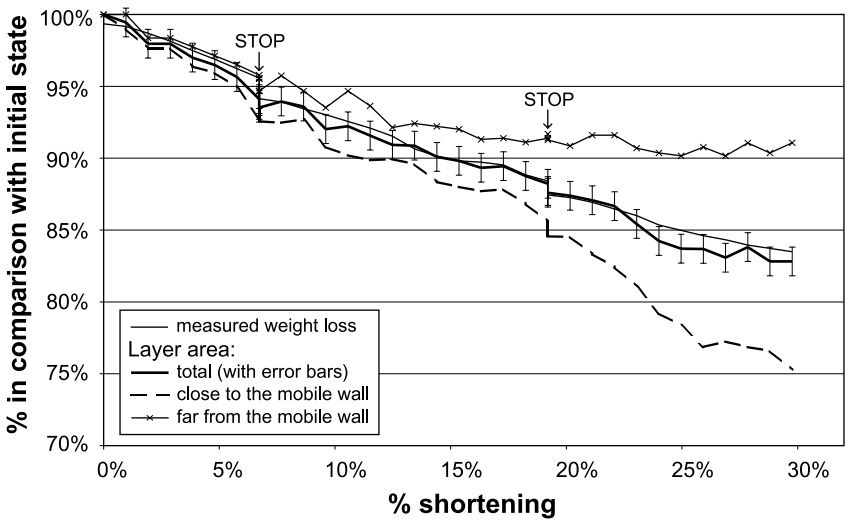

Fig. 8. Area loss measured on the photographs of the melt-bearing model. The layer was virtually separated into two parts, whose areas were equal before deformation. Error bars are ± 1% and are displayed only on the total area curve. Error is about the same for the other curves but no bars are shown for clarity. The small increases of area values correspond to fluctuations within error bars but are artificial. 'Stop' indicates a static interval. A good agreement exists between weight loss (Fig. 7) and total area loss. Melt expulsion is stronger close to than far from the mobile wall. After 15% shortening the non-folded part far from mobile wall did not lose any more melt while expulsion increased in intensity in the folding part.

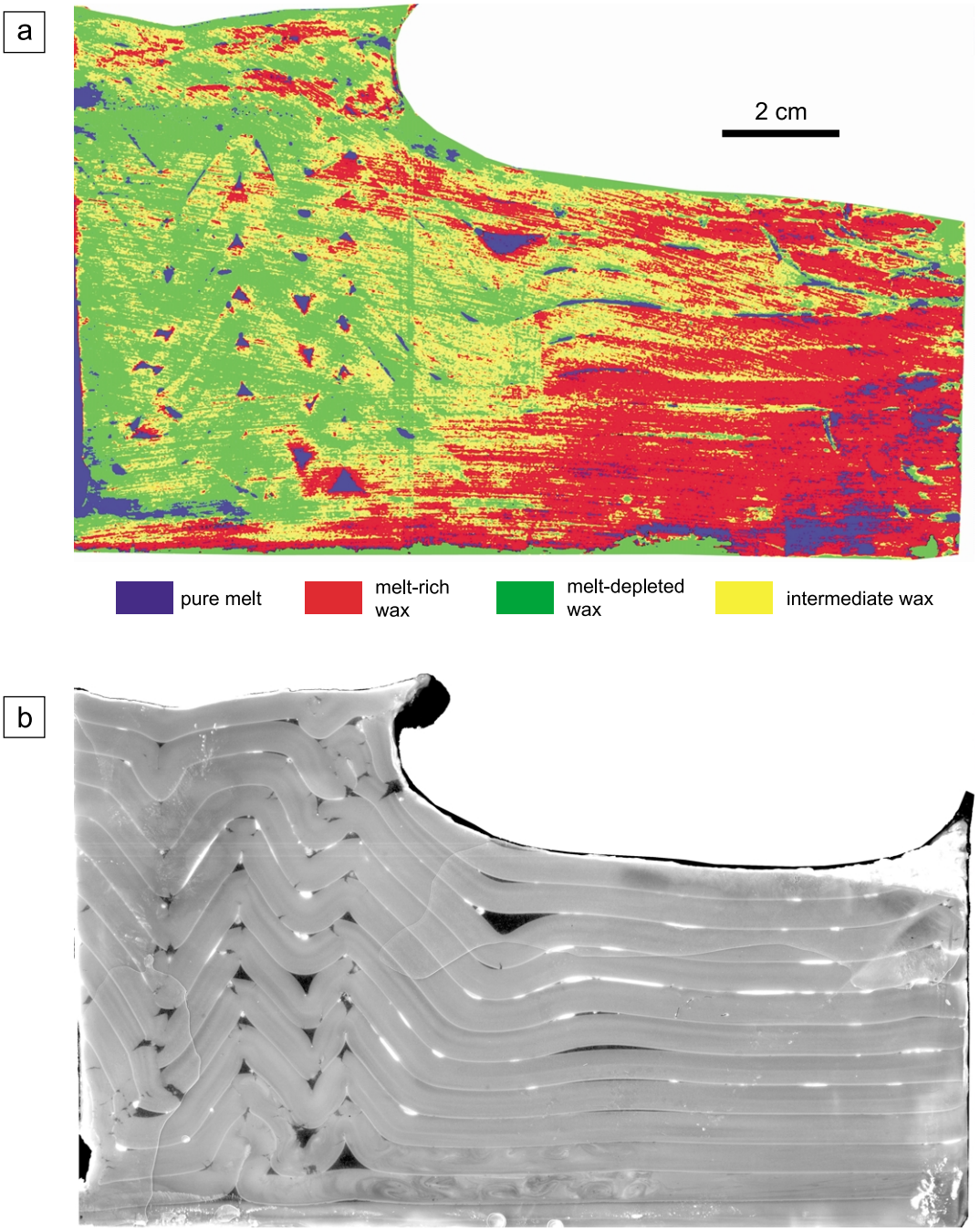

Fig. 9. Cross-sections in a model obtained in the same initial conditions as the melt-bearing experiment of Fig. 5. (a) The colour of the wax was classified by image processing into four categories as a function of melt content. The picture shows that folding was efficient in expelling melt from the partially molten material. Note the melt enrichment at the outer hinge zones of the folds. (b) Same cross-section after a surface treatment that removed the colour gradients of the wax but increased the contrast between the layers. Black veins are filled with crystallized melt. Bright dots and lines are voids created by contraction during cooling. They are supposed to contain melt during the experiment.

occurs by porous flow through the microscopic porosity of the wax. Pressure gradients are likely to build up between a vein and its deformed and compacted surroundings (Simakin and Talbot, 2001).

Once in a vein, the liquid is unable to go back into the compacted wax and must use the larger-scale vein network. Indeed, the melt-depressed surrounding of a vein has a low permeability so that the pressure of the melt in the vein must exceed the surface tension between crystals to percolate through the wax. In contrast, a vein can easily propagate laterally thanks to stress concentration at the tips.

The migration through the veins may occur either in an active or a passive way (Fig. 10). The passive driving mechanism of melt migration is based on the development and modification of the vein network during folding (Fig. 10a). This is the main mechanism in our experiments.

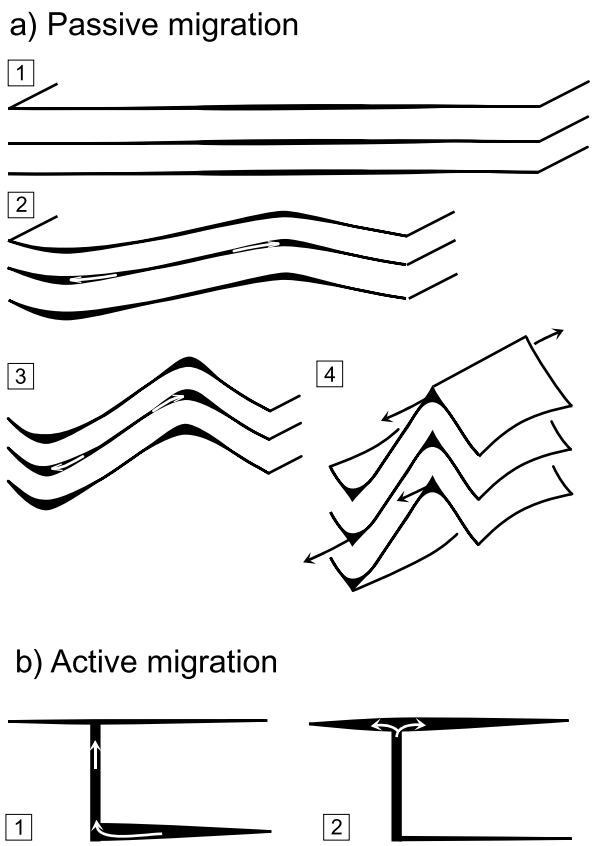

Fig. 10. Schematic representation of the passive (time sequence A) and active (time sequence B) melt migration processes that were observed in our analogue experiments. Black represents melt or magma; the partially molten material is white. 'Active' migration means that melt moves thanks to its intrinsic properties (low density and viscosity). In the 'passive' migration mechanism, the segregated melt follows the evolution of the geometry of foliation-parallel veins. During folding, melt may move from the limbs to the hinge, and then along the fold axis (arrows). This process makes it possible to expel melt from a deforming partially molten unit without full interconnection of the vein network.

Thanks to its low viscosity, melt follows the modifications of the vein geometry during folding. Closure at one end of a vein takes place together with opening at the other end. Hence, as shortening progresses, melt is constantly redistributed within the folding unit (Fig. 10a). The migration is said to be passive because the far-field stress field plays a major role in this mechanism: it causes the layer to shorten and fold, irrespective of the presence of melt or not; in return, the changes in the geometry of the vein network create the pressure gradients that drive the melt. In other words, the driving force of melt migration is not due to an intrinsic property of the melt (its low density), but is directly related to the strain rate gradients that build up between the different parts of the fold. Strain rate gradients are the rate form of strain gradients, that is to say a mathematical expression of the deformation heterogeneity.

Conversely, active migration means that melt moves, thanks to both its low density and low viscosity, from a source to a sink that are connected together (Fig. 10b). In this case, a far-field differential stress is not necessary. In our melt-bearing experiments this process takes place for example when a vein is connected by the sideways vertical spaces to the external water tank.

As seen previously, the efficiency of melt expulsion during folding increases with strain (Fig. 8). As shortening increases weakening of the axial plane region is likely to occur because of higher strain and increasing melt fraction. Opening of radial cracks at the outer arcs of the layers emphasises this phenomenon. These softer zones are therefore more compactible and expel their melt easily with further shortening. Hence, the axial planes start as melt-rich zones and highly permeable pathways, but at high strain, after lock-up and flattening, they are melt-depleted because of efficient melt expulsion.

Finally, the above process of melt migration during folding can be viewed as a sequence of two mechanisms: accumulation (generation of porosity) and expulsion (destruction of porosity). Each of these mechanisms is strain-dependent and may occur simultaneously at different places. The development of a train of folds implies a strong heterogeneity of strain. The episodic nature of the melt expulsion may therefore arise from the random occurrence of accumulation in dilating veins and expulsion in closing veins.

5. Field observations of folded migmatites

The aim of this section is to present some natural examples to which our experimental results may apply. These examples from the French Variscan Massif Central show foliation-parallel leucosomes that are thicker and more numerous in the hinge than in the limbs of folds (Fig. 11). Different shapes can be distinguished: triangle (Fig. 11a), lensoid pods (Fig. 11b) and crescent (Fig. 11c). Triangle- and crescent-shaped saddle reefs have been observed in the melt-bearing experiment (Fig. 5). Similar examples can be found in the literature (e.g. figs. 2d and 3c in Vanderhaeghe, 2001; fig. 6 in Rosenberg et al., 1995; figs. 3b and 6d (bottom) in Marchildon and Brown, 2003). It is worth noticing that: (1) these features are distinct from (discordant) axial-surface leucosomes (e.g. Vernon and Paterson, 2001); (2) all migmatites do not exhibit this relationship between folds and leucosomes. Nevertheless, these examples show that our analogue experiments produced realistic geometries.

The saddle reef geometry of granitic bodies occurs also at larger scales in anatectic domains: Allibone and Norris (1992) described concordant leucogranite microplutons, 50 m wide, emplaced in the hinge zones of anticlines beneath impermeable amphibolite layers; they suggested that melt segregated and migrated from the fold limbs. Kisters et al. (1998) described in South Africa a close association of brecciated host-rock material with diatexites or granites in the axial zone of anticlines and showed that zones of higher strain had focused melt migration.

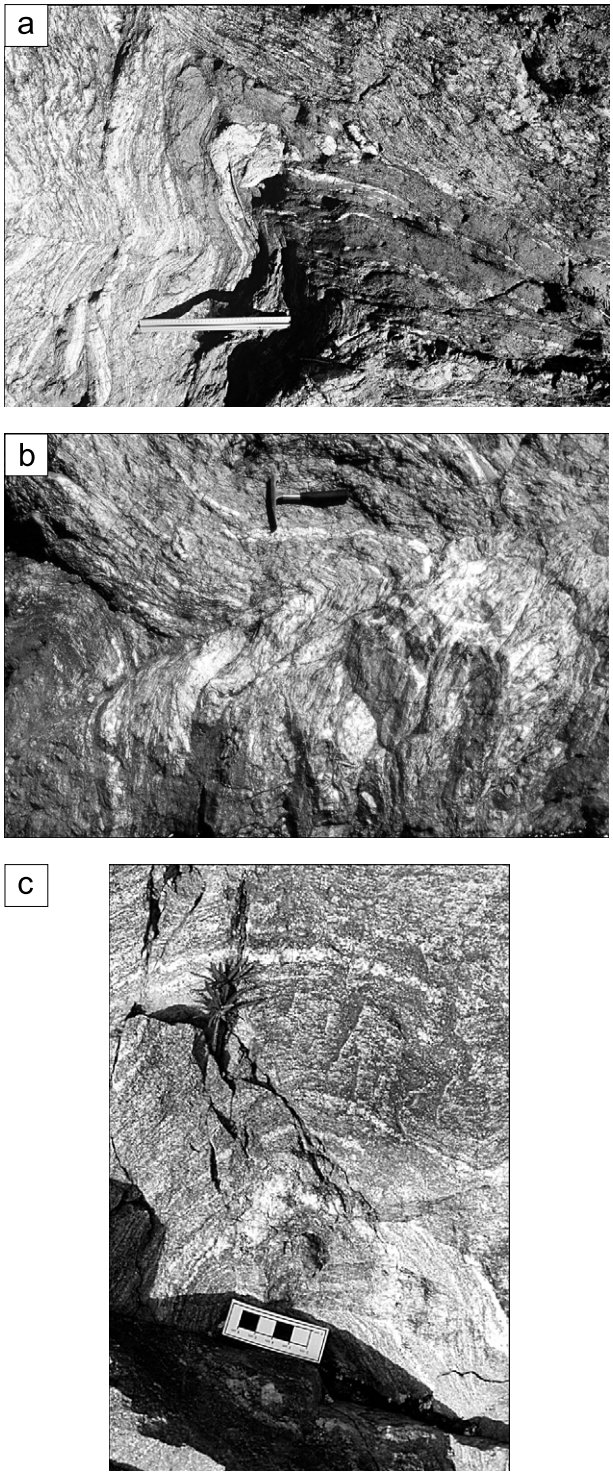

Fig. 11. Folds and leucosomes in migmatitic rocks. In all cases the protolith is a biotite-rich paragneiss and the cited authors have demonstrated the synchronism between deformation and migmatization. (a) Folded migmatitic paragneiss of the migmatitic rim in the south of the Velay dome, Variscan French Massif Central, Pont de Bayzan outcrop (Montel et al., 1992). A cylindrical leucosome with saddle reef geometry occupies the core of an antiform. This leucosome has two 'legs', which are the centimetre-thick foliation-parallel leucosomes running down the limbs. The scale is 40 cm long. (b) Same outcrop as (a) but the picture shows a more diffuse gathering of leucosomes in the axial plane. (c) Folded migmatite in the Upper Gneiss Unit, leptyno-amphibolitic complex, French Massif Central (Gardien et al., 1990). The leucosomes are crescent-shaped, their thickness increasing from limbs to hinge. The black and white squares are 2 cm by 2 cm.

6. Discussion

6.1. Boundary conditions

Even if we carefully scaled our experiments, the simple projection of our results to natural migmatites is not possible because (1) nature is much more complex than our analogue model (but simplification allows us to isolate relevant issues), and (2) the boundary conditions are simplistic. Boundary conditions refer here to the geometry of the box, to the kinematic conditions applied at the edges of the model, and to the multilayered structure of the model.

The vertical sides of the box acted as vertical conduits for melt expulsion. In nature, these vertical planes would for example correspond to boundaries of vertical shear zones perpendicular to fold axes. At the kilometre scale, these shear zones are expected to be efficient melt pathways to higher structural levels (Hollister and Crawford, 1986; Handy et al., 2001). In transpressional settings, such vertical shear zones kinematically link horizontally shortened domains. Even if these shear zones are ordinarily oblique to fold axes, we assume that our model does document the transition from horizontal to vertical melt migration in folding migmatites. At the metric scale, vertical discordant granite sheets are often described as melt-escape structures or pathways allowing opening of the system and melt extraction (Sawyer, 2001; Vanderhaeghe, 2001; Marchildon and Brown, 2003). As tension gashes, they preferentially form parallel to the shortening direction and so may virtually correspond to the long vertical edges of our analogue model. The difference with shear zones is that there are no displacements on these planes. Consequently, the analogy between discordant granite sheets and the vertical sides of the box is not kinematically correct, but remains useful.

The multilayered structure of our model implies that the prototype is a homogeneous material with discrete and regularly spaced planes of weakness. The base of the model is one of these planes; in the experiment, it played the role of a décollement above which horizontal shortening occurred. These planes of weakness may correspond in nature to slight differences in the modal composition of the rock, namely an increase in the mica content. This sort of prototype may be found in metamorphosed sedimentary units where primary features such as compositional layering have been preserved. As Sawyer (2001) pointed out, when the melting reactions involve the dehydration of micas, proto-leucosomes form thin foliation-parallel films. Inhomogeneous mica content will then result in discrete spatial distribution of weak planes lubricated by melt.

From a mechanical point of view, the initial structure of

our wax layer implies that the shear and tensile strength tensors were anisotropic. As discussed by many authors (e.g. Wickham, 1987; Cosgrove, 1997; Handy et al., 2001), two tensile strengths may be defined for foliated rocks, i.e. for fracturing oblique and parallel to the layering, the latter being the lowest one. The easy shear on the planar interface between two sub-layers is best described by a low yield limit. We could not measure these three parameters for our model but they were obviously lowered by the presence of melt. Besides, a decrease of the solid matrix viscosity because of increased temperature was likely. However, as the mechanical behaviour was dominated by strain localization (vein opening and layer boundary sliding), we can conclude that the decrease of the solid matrix viscosity is relatively not important.

In summary, the boundary conditions of our experiments emphasize the importance of mesoscale properties of migmatites compared with grain-scale features such as melt topology, textures and modal composition. Although the latter parameters are highly relevant, our experiments show that the mesoscale temporal and spatial evolution of the leucosome network is as important in explaining melt migration. These points are discussed in the following sections.

6.2. Foliation-parallel leucosomes

Foliation-parallel leucosomes are common in migmatites. The numerous models proposed to explain their generation can be divided into two families depending on whether or not they involve the role of differential stress.

In the first family, the migmatitic banding (leucosomes + mesosomes ± melanosomes) reflects the initial compositional layering of the protolith because melting reactions are dependent on the mineral (Sawyer, 2001) or water content (Johannes and Gupta, 1982). These models account for the regular layering of many stromatic migmatites. However, they do not explain: (1) why a homogeneous protolith would show a migmatitic banding after migmatization, (2) why leucosomes are often lensoid and discontinuous, or (3) why leucosomes concentrate in shear zones or axial planes of folds.

The second family of models suggests that leucosomes form in association with pressure gradients due to application of stresses to rheologically contrasted materials. Two models have been proposed, depending on the orientation of the maximal principal stress with respect to the leucosome.

In the first model, a layer-normal compression drives the mobile phase (fluids or melt) from incompetent to competent layers because competent layers support larger differential stress and have lower mean stress (Robin, 1979; Brown et al., 1995). If leucosomes contain large stiff crystals of quartz, Brown et al. (1995) argued that they are more competent than the mica-rich surrounding layers. Melt thus moves to leucosomes and emphasises a migmatitic banding. This mechanism stops when the growing melt fraction of leucosomes has reduced the viscosity contrast too much to allow further melt segregation. This model requires a constant layer-normal compression, for instance gravity applied on horizontal layering. It fails, therefore, to account for syntectonic melt segregation in typical folded stromatic migmatites that present vertical, horizontal and folded leucosomes in the same outcrop.

In the second model, the layer-parallel compression of an anisotropic and heterogeneous material like migmatites leads to heterogeneous deformation, which may create pressure gradients. Melt is thus driven from compacting domains to low-pressure sites (Sleep, 1988; Petford, 1995; Rutter and Neumann, 1995; Simakin and Talbot, 2001). At the grain scale, this deformation-assisted model finds its justification in the analogue experiments by Rosenberg and Handy (2000) that show the movement of the melt from pores to external larger pools in a deforming partially molten sample. At the metre and hectometre scales, our experiments suggest that 5% foliation-parallel shortening is enough to form foliation-parallel leucosomes (Fig. 5b). Some of the layering-parallel veins produced in our experiments have a very high aspect ratio (1 mm thick and 15 cm long). With a length ratio of 100 between the model and nature, the corresponding natural foliation-parallel leucosomes would be 10 cm thick and 15 m long; such examples have been shown by Mengel et al. (2001). A length ratio of 10 would account for leucosomes 1 cm thick and 1.5 m long, which are typical of stromatic migmatites (e.g. Mehnert, 1968; Johannes and Gupta, 1982; Marchildon and Brown, 2003).

A foliation-parallel shortening of 5% is probably difficult to recognise in the field since it is not enough to re-orient the foliation or to produce folds. However, it may suffice to open pre-existing planes with low cohesion such as foliation planes, especially those already coated by melt. We put the emphasis on the fact that spectacular granite-filled structures such as inter-boudin partitions and shear bands are not the only evidence of the tectonic control of melt distribution in migmatites.

6.3. Saddle reefs in migmatites

Saddle reefs occur usually in low-grade metasedimentary settings; they are generally filled with quartz or calcite (e.g. Ramsay and Huber, 1987) and may extend for a considerable distance along strike (Jessell et al., 1994). The mineralization that can be associated with these dilatant veins suggests that they are the seat of intense syntectonic fluid flow (Windh, 1995).

Saddle reefs are typically found in chevron folds and are mostly triangular shaped. However, in this paper, the term has been taken in a broader sense and every layer-parallel vein that is thicker at the fold hinge is called a saddle reef, whatever the shape of the fold. Our field examples of folded layered migmatites thus show several differences with

chevron folds: thickened hinge and thinned limbs (Fig. 11a); cuspate-shaped inner arcs (Fig. 11a and b); broad hinge zones (Fig. 11b and c); and sinusoidal open profiles (Fig. 11c).

Several questions may arise at that point: are saddle reefs common in folded stromatic migmatites? How do they form? Can they be used as an indicator of syntectonic melt migration?

As previously noticed, gathering of leucocratic material in the axial region of folds is not exceptional in anatectic domains. A comprehensive review of the relationships between folds and leucosomes is not the purpose of this paper. In fact, the relevant issue is not to know if saddle reefs exist in migmatites but to explain why they occur sometimes. Because of their potential importance in melt migration processes, it is worth thinking about their formation, which likely involves many coupled processes such as folding mechanisms and deformation-assisted porous flow.

As summarised by Fowler (1996) for folded low-grade metasediments, opening of bedding-parallel veins may occur before or during folding. In the first case, the saddle reef geometry will be acquired after the vein formation by folding and thickening in the hinge zone (host rock plus vein)—the vein must therefore undergo internal strain. In the second case, the opening of the vein and its shaping into saddle-reef geometry are synchronous with folding. Opening of voids is due to incompatible deformation between adjacent layers during the rotation of the limbs. In ideal chevron folds, triangular voids open in narrow hinge zones because layer-parallel shear displacements increase from a competent layer to an adjacent incompetent layer (Ramsay and Huber, 1987). Chevron folds are flexural folds and can actually be formed by two different mechanisms: (1) *flexural slip*, involving discrete movement horizons and discontinuous shear-displacements variations (Tanner, 1989); (2) *flexural flow*, involving welded layers and continuous shear displacements variations (Ramsay and Huber, 1987). Of course, a combination of the two processes is possible. Furthermore, Smith and Marshall (1993) pointed out that flexural folding is not the only way to open saddle reefs and they presented a mechanism called *compatible folding*. In this model, the layers maintain contact at the limbs and opening in hinges occurs because the amount of stretch parallel to the axial surface is constant throughout the fold profile, i.e. from hinge zones to limbs zones. A low interlayer cohesion is required in this model.

Although chevron folds are present in our melt-free experiment, saddle reefs are absent. Moreover, our melt-bearing experiment shows saddle reefs both in open sinusoidal folds and in tight chevron folds (Figs. 5 and 6). The presence of saddle reefs is therefore not linked to a particular style of fold. The only difference between our two experiments is the presence of melt, which lowers the yield limits of layer-parallel fracturing and slip. These decreases of strength are emphasised by the early segregation of melt in layer-parallel veins. The following sequence is then visible: (1) opening of crescent-shaped saddle reefs in open sinusoidal folds, (2) transformation of open folds into chevron folds—then saddle reefs become triangular. The first stage involves the compatible folding mechanism of Smith and Marshall (1993), while the second stage involves flexural-slip folding.

Deformation-enhanced fluid-transport processes may be similar in both metasedimentary and migmatitic settings because compaction, hydraulic fracturing and fluid-enhanced strain localisation are partly controlled by the low viscosity of the fluid (aqueous fluid or silicate melt) relative to the solid matrix (Vigneresse et al., 1996; Holness, 1997). Consequently, we may expect folding to produce comparable geometries in both settings. Nevertheless, conditions should be similar to the ones that prevail in our melt-bearing experiment: a layered structure with discrete planes of weakness and a moderate fluid proportion.

The comparison between the experimental results and nature has some limits since the layered structure of stromatites may vanish when the melt content exceeds a critical percentage (e.g. Vanderhaeghe, 2001). This threshold has been the subject of many studies and its value may vary between 10 and 60 vol.% (see Renner et al. (2000) and Rosenberg (2001) for recent discussions). Even if the melt percentage was about 30 vol.% in our analogue model, wax still kept its cohesion and our experiment was therefore conducted well below a supposed rheological threshold. In contrast, migmatites may undergo a transition from metatexites (the foliation still dominates the mechanical behaviour) to diatexites (the anisotropic structure is lost) that is not reproduced in our analogue model. A large range of deformation styles produced at high melt content (convoluted folds, patchy migmatites, etc.) remains therefore beyond the scope of our model.

Leucosomes that are thicker in the hinge may also form by solid-state hinge thickening. They may be very difficult to discern from synmagmatic saddle reefs. The presence or absence of an axial plane schistosity is not a sound criterion since schistosity can develop in partially molten rocks (Rosenberg and Handy, 2000). Moreover, the potential absence of solid-state deformation in synmagmatic folds may be misleading since recrystallisation may produce equilibrated textures even in folded subsolidus high-grade rocks. Our experiments suggest finally that the presence of saddle reefs in migmatites can be used as an indicator of synmagmatic folding, not as an unequivocal criterion.

6.4. Expulsion mechanisms in migmatites

Our experiments suggest that the expulsion of melt from deforming migmatites may be a multistage mechanism involving two distinct networks at different scales. In nature, the microscopic network consists of pores and interconnected melt films at boundaries between crystals (Rutter and Neumann, 1995; Sawyer, 2001). The melt movement in this

grain-scale network occurs over small distances and is assisted by compaction (Rutter and Neumann, 1995; Simakin and Talbot, 2001). Melt moves from the microscopic to the mesoscopic network, the contrary being either impossible or very slow. This single sense of movement has already been noticed for our wax model and we can add that, in many migmatites, foliation-parallel veins are coated by micas that greatly decrease the permeability in the direction normal to foliation (Laporte and Watson, 1995). The melt may therefore migrate through networks on an increasing scale. Sawyer (2001) reached a similar conclusion by comparing textures in melt-depressed and melt-enriched layers in migmatites. It follows that, once the mesoscale network is formed, it evolves independently from the microscopic one.

There are two important consequences of our 'dilatancy-collapse' mechanism of melt migration. First, melt-flow conduits may disappear, especially in zones of flattening-to-plane strain. The apparent network of leucosomes in exposed migmatites may not necessarily reflect the actual pathways followed by the melt. Second, the melt-flow network does not need to be fully interconnected to allow expulsion. On the mesoscale, interconnection means that highly oblique veins must regularly connect isolated foliation-parallel channels (e.g. Rutter and Neumann, 1995; Vanderhaeghe, 1999). Melt flow in such a vein network may be considered as a mesoscale Darcy flow with high permeability, allowing fast and efficient melt transport (Rutter and Neumann, 1995). However, long-lived fully interconnected networks may be rather exceptional and migmatites may be melt-depleted even though they do not exhibit a pervasive family of crosscutting fractures (Sawyer, 2001; White and Powell, 2002). Our deformation-assisted mechanism allows melt-filled pockets to move by following the changing orientation of anisotropic structures (foliation, fold axes). Hence, folding migmatites may episodically feed discrete and remote vertical conduits.

Consequently, the time-scale of mesoscale melt migration in moving veins is of the order of magnitude of the time necessary to develop folds in migmatites. A direct and simple application of our experimental results to nature consists in calculating the time necessary to expel 50% of the melt from a folding migmatized layer, i.e. the time to shorten a layer by one third. It takes between 10^4 and 10^6 years if strain rate is in the range 10^{-12}–10^{-14} s^{-1}.

7. Conclusions

Layered migmatites are modelled with thin superposed layers of partially molten wax. Their main characteristics and mechanical properties are reproduced: anisotropic tensile and shear strengths, a moderate fraction (30 vol.%) of a melt with negative buoyancy and with very high viscosity contrast with its solid matrix. A variety of settings can be reproduced on scales between the centimetre and the hectometre.

Melt-filled veins with high aspect ratios are produced during layer-parallel shortening. They open along foliation as soon as the shortening begins. The melt is segregated from the surrounding matrix into the veins, forming a stromatic layering. These veins are highly conductive planar flow paths. If the system is open, the melt migrates along them and begins to escape.

During incipient folding, crescent-shaped saddle reefs open in the hinges of open sinusoidal folds. With further shortening chevron folds develop and the saddle reefs become triangular because shear displacements on the interfaces between the layers are enhanced by the presence of melt. In comparison, a melt-free experiment shows few layer-parallel veins and no saddle reefs in chevron folds.

The axial planes of folds take, successively, the role of accumulation sites, melt pathways and melt-depressed zones. Strain softening is assumed to occur close to the axial planes because of higher melt content. It follows that strain, compaction and melt expulsion are increasingly localised in axial planes of folds.

The geometry of the mesoscale melt-flow network constantly changes during folding, which creates the pressure gradients that drive melt migration. As a result, melt loss is higher in folding migmatites than in static ones. Mesoscale melt migration is a combination of flow in immobile veins and movements of veins as a whole. The melt-flow network does not need to be interconnected to allow expulsion. Melt movement occurs in pulses and melt expulsion is episodic because the strain/time dependence of the network evolution combines with the spatial heterogeneity of the deformation.

Acknowledgements

We thank C.J. Talbot, M. Brown and an anonymous reviewer for their very helpful comments and suggestions. We also gratefully acknowledge O. Vanderhaeghe for his remarks on an earlier draft of the manuscript.

References

Abbassi, M.R., Mancktelow, N.S., 1992. Single layer buckle folding in non-linear materials. I. Experimental study of fold development from an isolated initial perturbation. Journal of Structural Geology 14, 85–104.

Allibone, A.H., Norris, R.J., 1992. Segregation of leucogranite micro-plutons during syn-anatectic deformation: an example from the Taylor Valley, Antarctica. Journal of Metamorphic Geology 10, 589–600.

Barraud, J., Gardien, V., Allemand, P., Grandjean, P., 2001a. Analog modelling of melt segregation and migration during deformation. Physics and Chemistry of the Earth Part A 26, 317–323.

Barraud, J., Gardien, V., Allemand, P., Grandjean, P., 2001b. Strain-dependence of the melt migration in partially molten crustal rocks. Journal of the Virtual Explorer 4 http://virtualexplorer.com.au.

Brown, M., 1994. The generation, segregation, ascent and emplacement of

granite magma: the migmatite-to-crustally-derived granite connection in thickened orogens. Earth-Science Reviews 36, 83–130.

Brown, M., Solar, G.S., 1999. The mechanism of ascent and emplacement of granite magma during transpression: a syntectonic granite paradigm. Tectonophysics 312, 1–33.

Brown, M., Averkin, Y.A., McLellan, E.L., Sawyer, E.W., 1995. Melt segregation in migmatites. Journal of Geophysical Research 100, 15655–15679.

Cosgrove, J.W., 1997. The influence of mechanical anisotropy on the behaviour of the lower crust. Tectonophysics 280, 1–14.

Dorset, D.L., 1997. Crystallography of waxes—an electron diffraction study of refined and natural products. Journal of Physics D: Applied Physics 30, 451–457.

Fowler, T.J., 1996. Flexural-slip generated bedding-parallel veins from central Victoria, Australia. Journal of Structural Geology 18, 1399–1415.

Gardien, V., Tegyey, M., Lardeaux, J.M., Misseri, M., Dufour, E., 1990. Crustal-mantle relationships in the French Variscan chain: the example of the southern Monts du Lyonnais unit (eastern French Massif Central). Journal of Metamorphic Geology 8, 477–495.

Gardien, V., Thompson, A.B., Grujic, D., Ulmer, P., 1995. Experimental melting of biotite + plagioclase ± muscovite assemblages and implications for crustal melting. Journal of Geophysical Research 100, 15581–15591.

Grujic, D., Mancktelow, N.S., 1995. Folds with axes parallel to the extension direction: an experimental study. Journal of Structural Geology 17, 279–291.

Handy, M.R., Mulch, A., Rosenau, M., Rosenberg, C.L., 2001. The role of fault zones and melts as agents of weakening, hardening and differentiation of the continental crust: a synthesis. In: Holdsworth, R.E., Strachan, R.A., Magloughlin, J.F., Knipe, R.J. (Eds.), The Nature and Tectonic Significance of Fault Zone Weakening. Geological Society 186, pp. 305–332

Holness, M.B. (Ed.), 1997. Deformation-enhanced Fluid Transport in the Earth's Crust and Mantle, Chapman & Hall, London.

Jessell, M.W., Willman, C.E., Gray, D.R., 1994. Bedding parallel veins and their relationship to folding. Journal of Structural Geology 16, 753–767.

Johannes, W., Gupta, L.N., 1982. Origin and evolution of a migmatite. Contributions to Mineralogy and Petrology 79, 114–123.

Kisters, A.F.M., Gibson, R.L., Charlesworth, E.G., Anhaeusser, C.R., 1998. The role of strain localization in the segregation and ascent of anatectic melts, Namaqualand, South Africa. Journal of Structural Geology 20, 229–242.

Kriegsman, L.M., 2001. Partial melting, partial melt extraction and partial back reaction in anatectic migmatites. Lithos 56, 75–96.

Hollister, L.S., Crawford, M.A., 1986. Melt-enhanced deformation: a major tectonic process. Geology 14, 558–561.

Laporte, D., Watson, E.B., 1995. Experimental and theoretical constraints on melt distribution in crustal sources: the effect of crystalline anisotropy on melt interconnectivity. Chemical Geology 124, 161–184.

Marchildon, N., Brown, M., 2003. Spatial distribution of melt-bearing structures in anatectic rocks from Southern Brittany, France: implications for melt transfer at grain- to orogen-scale. Tectonophysics 364, 215–235.

McKenzie, D., 1984. The generation and compaction of partially molten rock. Journal of Petrology 25, 713–765.

Mehnert, K.R., 1968. Migmatites and the Origin of Granitic Rocks, Elsevier, Amsterdam.

Mengel, K., Richter, M., Johannes, W., 2001. Leucosome-forming small-scale geochemical processes in the metapelitic migmatites of the Turku area, Finland. Lithos 56, 47–73.

Milord, I., Sawyer, E.W., Brown, M., 2001. Formation of diatexite migmatite and granite magma during anatexis of semi-pelitic metasedimentary rocks: an example from St. Malo, France. Journal of Petrology 42, 487–505.

Montel, J.M., Marignac, C., Barbey, P., Pichavant, M., 1992. Thermobarometry and granite genesis: the Hercynian low-P, high-T Velay anatectic dome (French Massif Central). Journal of Metamorphic Geology 10, 1–15.

Neurath, C., Smith, R.B., 1982. The effect of material properties on growth rates of folding and boudinage: experiments with wax models. Journal of Structural Geology 4, 215–229.

Nyman, M.W., Pattison, D.R.M., Ghent, E.D., 1995. Melt extraction during formation of K-Feldspar + Sillimanite migmatites, West of Revelstoke, British Columbia. Journal of Petrology 36, 351–372.

Oliver, N.H.S., 1996. Review and classification of structural controls on fluid flow during regional metamorphism. Journal of Metamorphic Geology 14, 477–492.

Petford, N., 1995. Segregation of tonalitic–trondhjemitic melts in the continental crust: the mantle connection. Journal of Geophysical Research 100, 15735–15743.

Ramberg, H., 1981. Gravity, Deformation and the Earth's Crust, Academic Press, London.

Ramsay, J.G., Huber, M.I., 1987. Modern Structural Geology. Volume 2: Folds and Fractures, Academic Press, London.

Renner, J., Evans, B., Hirth, G., 2000. On the rheologically critical melt fraction. Earth & Planetary Science Letters 181, 585–594.

Ricard, Y., Bercovici, D., Schubert, G., 2001. A two-phase model for compaction and damage. 2. Application to compaction, deformation, and the role of interfacial surface tension. Journal of Geophysical Research 106, 8907–8924.

Robin, P.-Y.F., 1979. Theory of metamorphic segregation and related processes. Geochimica et Cosmochimica Acta 43, 1587–1600.

Rosenberg, C.L., 2001. Deformation of partially molten granite: a review and comparison of experimental and natural case studies. International Journal of Earth Sciences 90, 60–76.

Rosenberg, C.L., Handy, M.R., 2000. Syntectonic melt pathways during simple shearing of a partially-molten rock analogue (norcamphor–benzamide). Journal of Geophysical Research 105, 3135–3149.

Rosenberg, C.L., Berger, A., Schmidt, S.M., 1995. Observations from the floor of a granitoid pluton: inferences of the driving force of final emplacement. Geology 23, 443–446.

Rutter, E.H., Neumann, D., 1995. Experimental deformation of partially molten Westerly granite under fluid-absent conditions with implications for the extraction of granitic magmas. Journal of Geophysical Research 100, 15697–15715.

Sawyer, E.W., 2001. Melt segregation in the continental crust: distribution and movement of melt in anatectic rocks. Journal of Metamorphic Geology 19, 291–309.

Simakin, A., Talbot, C., 2001. Tectonic pumping of pervasive granitic melts. Tectonophysics 332, 387–402.

Sleep, N.H., 1988. Tapping of melt by veins and dikes. Journal of Geophysical Research 93, 10255–10272.

Smith, J.V., Marshall, B., 1993. Implications of discrete strain compatibility in multilayer folding. Tectonophysics 222, 107–117.

Solar, G.S., Brown, M., 2001. Petrogenesis of migmatites in Maine, USA: possible source of peraluminous leucogranite in plutons? Journal of Petrology 42, 789–823.

Talbot, C.J., 1999. Can field data constrain rock viscosities? Journal of Structural Geology 21, 949–957.

Tanner, P.W.G., 1989. The flexural-slip mechanism. Journal of Structural Geology 11, 635–655.

Thompson, A.B., 1996. Fertility of crustal rocks during anatexis. Transactions of the Royal Society of Edinburgh: Earth Sciences 87, 1–10.

Vanderhaeghe, O., 1999. Pervasive melt migration from migmatites to leucogranite in the Shuswap metamorphic core complex, Canada: control of regional deformation. Tectonophysics 312, 35–55.

Vanderhaeghe, O., 2001. Melt segregation, pervasive melt migration and magma mobility in the continental crust: the structural record from pores to orogens. Physics and Chemistry of the Earth, Part A: Solid Earth and Geodesy 26, 213–223.

Vernon, R.H., Paterson, S.R., 2001. Axial-surface leucosomes in anatectic migmatites. Tectonophysics 335, 183–192.

Vigneresse, J.-L., Tikoff, B., 1999. Strain partitioning during partial melting and crystallizing felsic magmas. Tectonophysics 312, 117–132.

Vigneresse, J.-L., Barbey, P., Cuney, M., 1996. Rheological transitions during partial melting and crystallization with application to felsic magma segregation and transfer. Journal of Petrology 37, 1579–1600.

Weinberg, R.F., 1999. Mesoscale pervasive felsic magma migration: alternatives to dyking. Lithos 46, 393–410.

White, R.W., Powell, R., 2002. Melt loss and the preservation of granulite facies mineral assemblages. Journal of Metamorphic Geology 20, 621–632.

Wickham, S.M., 1987. The segregation and emplacement of granitic magmas. Journal of the Geological Society, London 144, 281–297.

Windh, J., 1995. Saddle reef and related gold mineralization, Hill End Gold Field, Australia: evolution of an auriferous vein system during progressive deformation. Economic Geology 90, 1764–1775.